Surface & Coatings Technology 405 (2021) 126570

Contents lists available at ScienceDirect

Surface & Coatings Technology

journal homepage: www.elsevier.com/locate/surfcoat

Influence of Si on tribological behavior of laser cladded Fe-based amorphous/crystalline composite coatings

Qianqian Wang [a], Xudong Bai [a], Bo Sun [a], Jian Liu [b], Zhihai Cai [b], Xiubing Liang [c,*], Baolong Shen [a,d,**]

[a] School of Materials Science and Engineering, Jiangsu Key Laboratory for Advanced Metallic Materials, Southeast University, Nanjing 211189, China
[b] National Engineering Research Center for Mechanical Product Remanufacturing, Academy of Army Armored Force, Beijing 100072, China
[c] National Institute of Defense Technology Innovation, Academy of Military Sciences PLA China, Beijing 100010, China
[d] Institute of Massive Amorphous Metal Science, China University of Mining and Technology, Xuzhou 221116, China

A B S T R A C T

By modifying the Si content, a $[(Fe_{0.6}Co_{0.2}Ni_{0.2})_{0.69}B_{0.2}Si_{0.11}]_{96}Nb_4$ amorphous/crystalline composite coating with high thermal stability and good tribological performance is fabricated by laser cladding on the Q235A steel. The coating has a Vickers hardness of 930 Hv, a high fracture strength above 2800 MPa, as well as a low wear loss of 3.77×10^5 μm^3 under a load of 10 N and a reciprocating frequency of 5 Hz after 30 min. The coating has a composition close to eutectic point, which leads to its large glass-forming ability and high amorphous fraction. The proper addition of Si also suppresses the formation and growth of dendritic grains. The good tribological performance of the coating comes from the high amorphous content and the refined crystalline structures.

1. Introduction

Coatings are widely applied in machinery, marine engineering and aerospace for surface modification and reparation. Amorphous alloys, which possess high hardness, good wear resistance [1,2] and excellent corrosion resistance [3,4] due to their short-range ordered and long-range disordered atomic arrangements [5,6], have become attractive potential coating materials for metal surfaces. Up to now, the investigations of multiple amorphous alloy systems as surface coating materials, including Fe- [7], Co- [8,9], Ni- [10], Zr- [11], Cu- [12], Al- [13,14], and Ti- [15] based amorphous alloys, have been reported. Among them, Fe-based amorphous coatings have attracted the most research attentions, not only because of their superiorities in low cost, extremely high hardness and strength, but also due to their excellent soft-magnetic properties that can be applied in magnetic shielding and electromagnetic materials. Several techniques have been developed to prepare Fe-based amorphous coatings, including plasma spray, laser cladding, spark cladding, and high velocity oxygen fuel (HVOF) [16–18]. During laser cladding process, the molten pool allows the coatings to be metallurgically bonded with the substrate to prevent failure at the interfaces, and the powders are completely melted during the cladding process to avoid formation of pores, both of which make the coatings reliable surface engineering materials with good wear and corrosion resistance [10,19]. Besides, with a relatively large cooling rate, laser cladding is a promising technique to prepare Fe-based amorphous coatings and suppress crystallization [20].

The attempt to prepare Fe-based amorphous coatings by laser cladding can be traced back to 1980s. During the last 40 years, the research in this area focused on optimizing the amorphous content, mechanical properties and corrosion resistance of coatings, mainly through composition modification and process optimization [21–23], and the past decade has witnessed the rapid development of laser cladded Fe-based amorphous coatings. FeNiSiBVM (M = Al, Ti, Mo and C) amorphous/crystalline composite coatings were prepared by laser cladding with low purity materials, and proper addition of the multicomponent is benefit to improve the glass-forming ability (GFA) [21]. The addition of Nb in laser cladded FeNiSiB coating improves its GFA and changes the crystallization behavior [24]. A large fraction of amorphous phase is detected in FeCrMoWMnCSi metallic glass composite coating produced by laser direct deposition, and both the hardness and wear resistance is improved by the amorphous phase [25]. The laser cladded FeCoCrMoCBY amorphous/crystalline coating exhibits excellent corrosion resistance due to the fine grains and the passive alloy elements [26]. By introducing FeCoCrMoCBY amorphous alloy into stainless steel using

* Corresponding author.
** Correspondence to: B. Shen, School of Materials Science and Engineering, Jiangsu Key Laboratory for Advanced Metallic Materials, Southeast University, Nanjing 211189, China.
E-mail addresses: liangxb_d@163.com (X. Liang), blshen@seu.edu.cn (B. Shen).

https://doi.org/10.1016/j.surfcoat.2020.126570
Received 30 September 2020; Received in revised form 26 October 2020; Accepted 28 October 2020
Available online 30 October 2020

selective laser melting, both the tensile strength and the corrosion resistance of the composite is improved [18]. However, the amorphous content of the laser-cladded Fe-based amorphous coatings still needs to be improved, and few report about their fracture strength has been made. It is well accepted that Si is a low-cost glass-forming element for Fe-based amorphous alloys due to the large negative mixing enthalpy (−35 kJ/mol) between Fe and Si [27]. Recent research in our group shows that Si can stabilize the supercooled liquid by promoting the formation of stable clusters with five-fold symmetries (icosahedral-like), which leads to the tremendous enhancement of the GFA for amorphous alloys even only with 0.5 at.% addition of Si. Thus, Si may play an essential role in the microstructure and mechanical performance of Fe-based amorphous coatings, which should be thoroughly studied.

FeCoNiBSiNb amorphous alloy, which has a large GFA and high strength [28], is a good candidate for surface coating materials. Preparation of FeCoNiBSiNb amorphous/crystalline composite coatings by laser melting has been reported before [1]. However, they only discussed the microstructure and tribological behavior of the coatings with and without metallic elements Co, Mo and Nb. The effect of the glass-forming element Si content hasn't been studied. In this work, the content of Si is modified in the FeCoNiBSiNb alloy system to produce $[(Fe_{0.6}Co_{0.2}Ni_{0.2})_{0.75-0.03x}B_{0.2}Si_{0.05+0.03x}]_{96}Nb_4$ (x = 0, 1, 2, 3, 4, 5 and 6 at.%) amorphous/crystalline composite coatings on a Q235A steel substrate by laser cladding. A detailed study of the microstructure, thermal behavior, as well as mechanical properties, including hardness, fracture strength and wear resistance of the coatings are carried out.

2. Experiments

Q235A steel with a dimension of 100 mm × 100 mm × 9 mm was used as the substrate. Before laser cladding, the substrate was polished using angle grinder and 800 mesh SiC sand paper, degreased using acetone and then vacuum dried at 80 °C. Powder mixtures with nominal compositions of $[(Fe_{0.6}Co_{0.2}Ni_{0.2})_{0.75-0.03x}B_{0.2}Si_{0.05+0.03x}]_{96}Nb_4$ (x = 0, 1, 2, 3, 4, 5 and 6 at.%) were selected for laser cladding. Fe powder, Co powder, Ni powder, Fe-B alloy powder (80.6 wt% Fe and 19.4 wt% B), Fe-Si (25 wt% Fe and 75 wt% Si), and Fe-Nb alloy powder (30 wt% Fe and 70 wt% Nb) were sieved (100 meshes). The purity of the powder is 99.9 wt%. The powder were then mixed evenly using ball-milling under vacuum atmosphere at a speed of 120 r/min for 12 h. The milling vial and milling balls are made of 304 stainless steel. The powder were then vacuum dried for 4 h at 80 °C. A 3 kW semiconductor laser was used to fabricate the coatings from the mixed powder using powder bed laser cladding under high purity argon gas shielding. The thickness of the powder on the substrate was 1 mm. The wavelength of the laser was 980 nm, and the laser spot was 14 mm × 2.5 mm rectangular-shaped. The laser scanning speed was 5 mm/s and the laser power was 2 kW.

Microstructure of the coatings was studied by X-ray diffraction (XRD, Bruker D8 Advance) with Cu *K*α radiation. The thermal properties of coatings were examined by differential scanning calorimeter (DSC, Netzsch 404 F3) at a heating rate of 40 K/min and a cooling rate of 4 K/min. The morphologies and elemental information of the coatings were analyzed by scanning electron microscope (SEM, FEI Sirion 200) equipped with an energy dispersive X-ray spectroscopy (EDS). For nanostructure analyses, the coatings were thinned carefully by a low-angle (5°) ion milling (GATAN-PIPS-M691) under liquid nitrogen cooling and then examined with a transmission electron microscope (TEM, FEI Tecnai G2 F20). The hardness was measured on the cross sections of coatings using a Vickers hardness tester (FUTURE-TECH FM-700). The fracture strength of coatings was measured by compressive tests using an electronic mechanical testing machine (Sans 5305) at a strain rate of $5 \times 10^{-4}\ s^{-1}$. The dimension of the samples for compressive tests were 0.5 mm × 0.5 mm × 1 mm, which were prepared through wire-electrode cutting followed by polishing.

The tribological properties of the coatings were studied using a friction wear testing machine (UMT-3) with a load of 10 N and 20 N. The Si_3N_4 ceramic ball with a diameter of 4 mm was used as the frictional counterpart. All of the samples were ground using 240 grits to 1000 grits abrasive papers. The dimension of the coating surface for wear tests is 10 mm × 7 mm. During the friction tests, all of the coatings were fixed and motionless, and the frictional counterpart is perpendicular to the coating surface. Dry sliding friction tests were carried out at room temperature with reciprocating distance of 4 mm. The sliding speeds are 40 and 80 mm/s, corresponding to the testing frequencies of 5 and 10 Hz, respectively. The apparatus was run for 30 min at each speed and load condition. The worn surfaces were analyzed using SEM. The volume losses after friction tests was obtained by the 3D interference surface topography instrument (ADE Phase shift MicroXAM-3D).

3. Results

3.1. Microstructure and thermal properties of the coatings

Microstructure of the as-cladded $[(Fe_{0.6}Co_{0.2}Ni_{0.2})_{0.75-0.03x}B_{0.2}Si_{0.05+0.03x}]_{96}Nb_4$ (x = 0, 1, 2, 3, 4, 5 and 6 at.%) coatings is analyzed by XRD, as shown in Fig. 1. All of the patterns show sharp diffraction peaks, revealing the existence of crystalline phases in the coatings. The crystalline phases in all of the coatings are identified as $Fe_2(B, Si)$, $Fe_3(B, Si)$ and α-(Fe, Co, Ni). Only small humps can be found at 45° of the XRD curves, which is usually the characteristic of Fe-based amorphous alloys. Since the humps are not distinct, it is difficult to evaluate the effect of Si content on the GFA of the coatings by calculating the fraction of amorphous phase using the Rietveld method [29]. Thus, DSC analyses were carried out to study not only the GFA but also the thermal stability of the coatings.

The melting and solidification processes of the as-cladded $[(Fe_{0.6}Co_{0.2}Ni_{0.2})_{0.75-0.03x}B_{0.2}Si_{0.05+0.03x}]_{96}Nb_4$ (x = 0, 1, 2, 3, 4, 5 and 6 at.%) coatings were analyzed using DSC. The cooling curves of DSC are shown in Fig. 2, and the values of characteristic temperatures of the coatings, including melting temperature T_m, liquidus temperature T_l, solidification starting temperature T_{s1}, solidification ending temperature T_{s2}, undercooling degree ΔT ($\Delta T = T_l - T_{s1}$) and solidification range ΔT_s, are listed in Table 1. As shown in Fig. 2, upon cooling, the coating with x = 2 only has one major exothermic peak with some satellite peaks on the

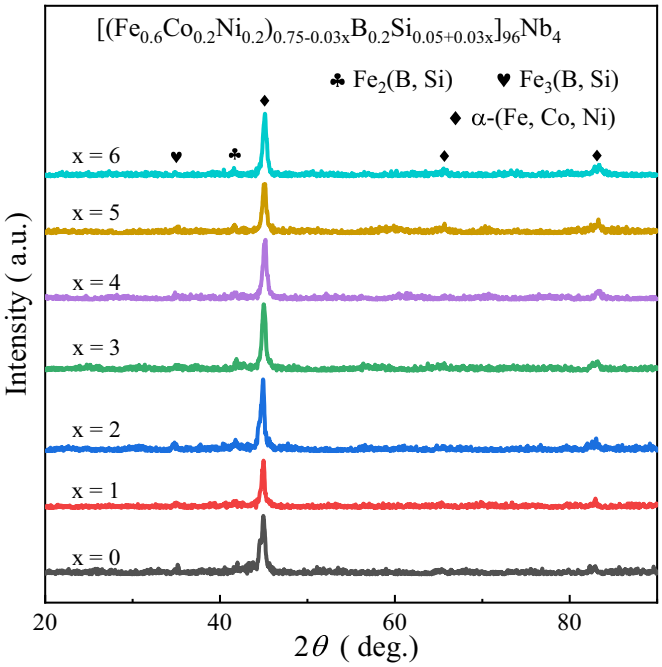

Fig. 1. XRD curves of $[(Fe_{0.6}Co_{0.2}Ni_{0.2})_{0.75-0.03x}B_{0.2}Si_{0.05+0.03x}]_{96}Nb_4$ (x = 0, 1, 2, 3, 4, 5 and 6 at.%) laser cladded coatings.

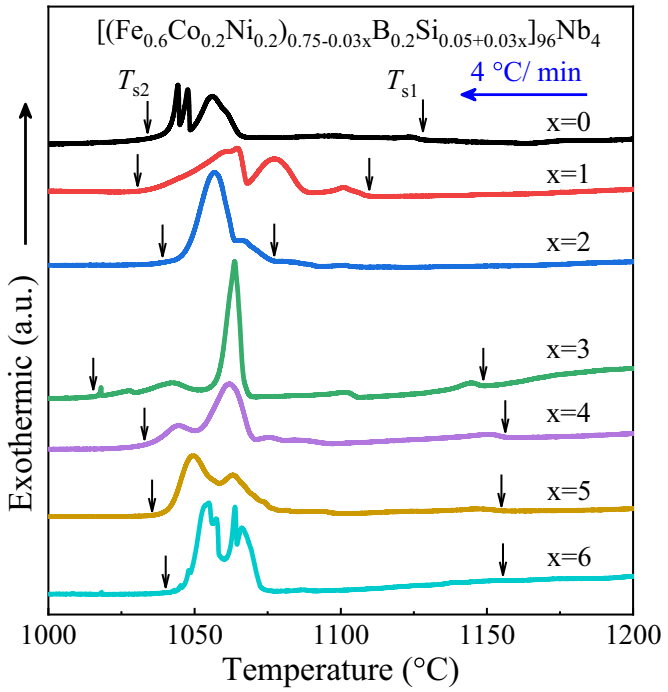

Fig. 2. Cooling curves of DSC for $[(Fe_{0.6}Co_{0.2}Ni_{0.2})_{0.75-0.03x}B_{0.2}Si_{0.05+0.03x}]_{96}Nb_4$ (x = 0, 1, 2, 3, 4, 5 and 6 at.%) laser cladded coatings.

shoulder, while all the other coatings exhibit more than three exothermic peaks. This result indicates that the coating with x = 2 is more close to the eutectic composition, or "deep eutectic", which reveals its better GFA according to the framework of phase competition [30]. Besides, the melting temperatures of the samples are within 1037 to 1058 °C, indicating the good thermal stability of the coatings. In contrary, the solidification starting temperature, which represents the starting temperature of the crystallization upon cooling, decreases firstly from 1130 to 1078 °C when x increases from 0 to 2, and then increases sharply to 1149–1160 °C with further addition of Si. As a result, when x = 2, the liquid is more stable than others as it has the largest degree of undercooling ΔT = 75 °C, also suggesting a better GFA of this coating [31]. In addition, the solidification range of the coating with x = 2 is the narrowest (48 °C), while that of the coating with x = 3 is the widest (134 °C). This indicates that the composition of coating with x = 3 is more far away from the eutectic point, also suggests the large temperature intervals between different precipitation phases. Thus, the coating with x = 2 has not only a better GFA, but also a more uniform phase distribution, while the coating with x = 3 has the most inhomogeneous structure.

As the coating with x = 2 has the best GFA, TEM analysis was carried out on it to study its nanostructure and to verify the existence of amorphous phase. As shown in Fig. 3, the TEM image shows representative areas of amorphous phase (the area between two red dashed lines) and crystalline phase. Besides, as shown by the selected area electron diffraction (SAED) pattern in the inset, not only crystalline diffraction dots but also blurring diffraction rings are observed, confirming the coexistence of the amorphous and crystalline phases. However, based on the TEM observations of different areas, the concentration of the amorphous phase is relatively small. This leads to that only small humps appear around 45°on the XRD curves. Based on the above results, a $[(Fe_{0.6}Co_{0.2}Ni_{0.2})_{0.69}B_{0.2}Si_{0.11}]_{96}Nb_4$ amorphous/crystalline composite coating is prepared using laser cladding.

3.2. Cross-sectional morphology of the coatings

The SEM images of the cross sections of $[(Fe_{0.6}Co_{0.2}Ni_{0.2})_{0.75-0.03x}B_{0.2}Si_{0.05+0.03x}]_{96}Nb_4$ composite coatings with x = 0, 2 and 4 are shown in the first, second and third rows of Fig. 4, respectively. The figures in the left and right columns are from the center parts and interfaces (between clad layer and substrate) of corresponding coatings, respectively. All the parts of the coatings are dense and nearly pore-free, indicating good quality of the coatings. Clearly, the microstructure of the coatings varies with Si contents. When x = 0, the center part of the coating is mainly composed of dendrite grains spreading all over the alloy matrix. As the image is enlarged, some randomly distributed smaller cellular crystals are observed near the dendrites, as shown in the inset of Fig. 4a, suggesting that the growth of some crystals were suspended during

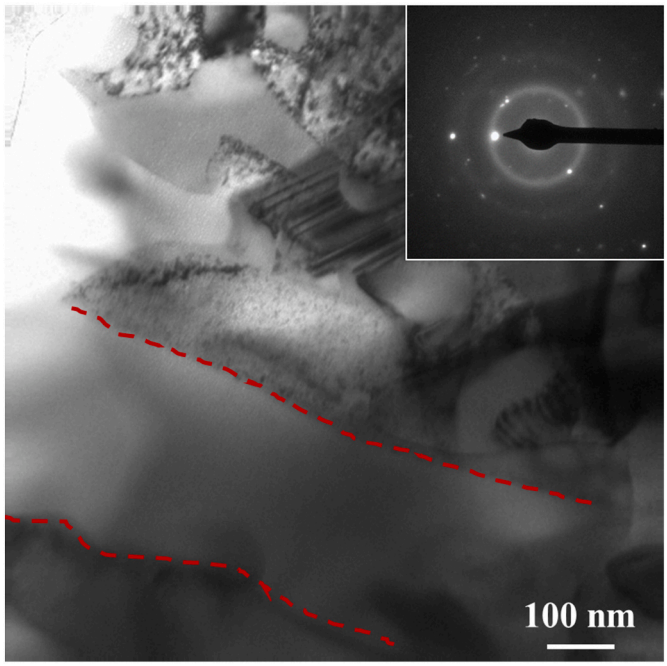

Fig. 3. TEM micrograph of the coating with x = 2, inset is the SAED pattern. (For interpretation of the references to color in this figure, the reader is referred to the web version of this article.)

Table 1
The thermal parameters and mechanical properties of $[(Fe_{0.6}Co_{0.2}Ni_{0.2})_{0.75-0.03x}B_{0.2}Si_{0.05+0.03x}]_{96}Nb_4$ (x = 0, 1, 2, 3, 4, 5 and 6 at.%) composite coatings. The wear loss is calculated after wear tests under a load of 10 N and a reciprocating frequency of 5 Hz for 30 min.

Si content	T_m (°C)	T_l (°C)	T_{s1} (°C)	T_{s2} (°C)	ΔT (°C)	ΔT_s (°C)	Hardness (Hv)	σ_f (MPa)	Wear loss (μm^3)
x = 0	1058	1158	1130	1027	28	103	719 ± 36	2130	5.2×10^5
x = 1	1050	1156	1111	1026	45	85	817 ± 27	2440	7.4×10^5
x = 2	1045	1153	1078	1030	75	48	930 ± 28	2875	2.1×10^5
x = 3	1037	1181	1149	1015	32	134	999 ± 101	2620	7.0×10^5
x = 4	1048	1190	1158	1027	32	131	1022 ± 39	2375	12.5×10^5
x = 5	1049	1177	1156	1034	21	122	1052 ± 27	2440	23.2×10^5
x = 6	1055	1178	1160	1041	18	119	1040 ± 71	2130	12.6×10^5

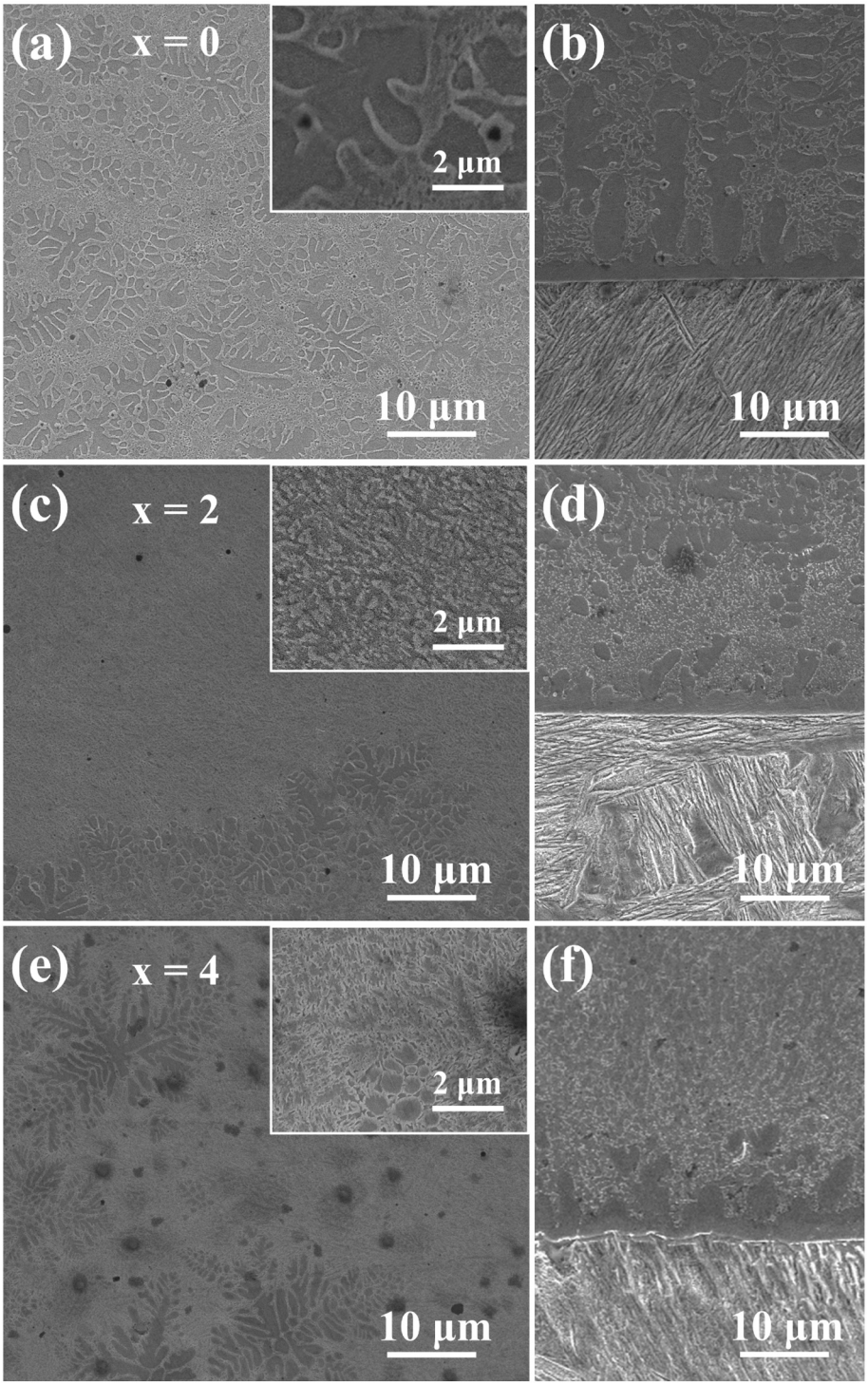

Fig. 4. SEM micrographs of the $[(Fe_{0.6}Co_{0.2}Ni_{0.2})_{0.75-0.03x}B_{0.2}Si_{0.05+0.03x}]_{96}Nb_4$ laser cladded coatings: the middle parts for (a) x = 0, (c) x = 2, (e) x = 4; the interfaces for (b) x = 0, (d) x = 2, (f) x = 4.

solidification. By slightly increasing the Si content (x = 2), the amount of dendrites in the center part of the coating is largely decreased, and the coating is mainly made of alloy matrix without obvious structural features, as shown in Fig. 4c. The enlarged image of the alloy matrix (as shown in the inset of Fig. 4c) reveals the coexistence of amorphous and cellular nanocrystalline phases. As shown in Fig. 4e, further addition of Si (x = 4) leads to a remarkable increase of the size of dendrites in the center part of coating. Based on the enlarged image in the inset of Fig. 4e, the areas without dendrites are composed of amorphous and cellular crystalline phases. It seems that the cellular crystals are growing by consuming the surrounding amorphous phase. Based on the above results, proper addition of Si (x = 2) results in the decrease of dendrites fraction and restriction of the cellular crystal growth.

As shown in Figs. 4b, d and f, no crack or pore was observed at the interfaces between the clad layer and the substrate for all of the three coatings. Besides, a thin layer of planar crystallites appear on the clad side next to the interface, confirming the metallurgical bond of the interfaces.

3.3. Wear properties of the coatings

The wear resistance is a decisive factor for the application of coatings. The wear resistance of the $[(Fe_{0.6}Co_{0.2}Ni_{0.2})_{0.75-0.03x}B_{0.2}Si_{0.05+0.03x}]_{96}Nb_4$ (x = 0, 1, 2, 3, 4, 5 and 6 at.%) amorphous/crystalline composite coatings are evaluated via the reciprocating ball-on-block dry-sliding wear tests, and compared with the Q235A substrate, with the results shown in Fig. 5. The 3D profiles of the worn surfaces for the composite coatings with different Si contents are plotted and compared with that of the substrate, as shown in Fig. 5a. All of the worn surfaces were analyzed after tested under 10 N at 5 Hz for 30 min. With the current testing parameters, the wear loss disparity for different coatings is manifested. The worn width and depth on the 3D profiles can reflect the wear resistance of the coatings visually. As the worn depth of the substrate is much larger than that for the coatings, the coatings share the same scale bar that is left to x = 6 coating, while the Q235A steel uses the scale bar next to itself. The worn depth of samples is enlarged 4 times for better visualizing. For the coatings, the width of worn surfaces decreases firstly when x increases from 0 to 2, and then increases with further Si addition. Similarly, the depth of the coatings decreases firstly and then increase, reaching the lowest value at x = 2. These observations indicate the wear properties can be modified by varying the Si contents, and the best wear resistance is achieved at x = 2. Besides, the worn width and depth of the Q235A is about 4 and 15 times larger than the coating with x = 2, revealing the great improvement in the wear resistant property for the surface after laser cladding treatment. Most of the worn surfaces are relatively smooth, except the coating with x = 6, which shows a few burrs on the 3D profile. The smaller (highlighted by black circles) and larger burrs (highlighted by red oval) come from plastic deformation and peeling-off pits, respectively, which reveals the relative low wear resistance of this coating. The observations from the 3D profile of worn surfaces after wear tests show that the coating with x = 2 has the best wear resistance.

The friction coefficient can reflect the contact condition between the sample surface and the grinding couple, i.e. the higher the friction coefficient, the more difficult the wear ball slides, and the more easily the adhesive wear occurs [32]. The friction coefficient curves as a function of wear time for the substrate and the coating (x = 2) are shown in Fig. 5b. The friction coefficients were obtained from the wear tests with reciprocating frequency of 5 Hz. When applied the same load (10 N), the coating exhibits a much lower friction coefficient than the substrate, revealing a better anti-friction property of the coating. For the same coating, it shows a lower friction coefficient under a heavier load (20 N), indicating a better friction resistance. However, the fluctuation of the friction coefficient for the coating is much larger when the load is 20 N, indicating the amount of wear loss increases under a heavier load. With a larger load, the interaction between the friction pairs is more strenuous and less stable, leading to continuous weight loss and the fluctuation of the friction coefficient.

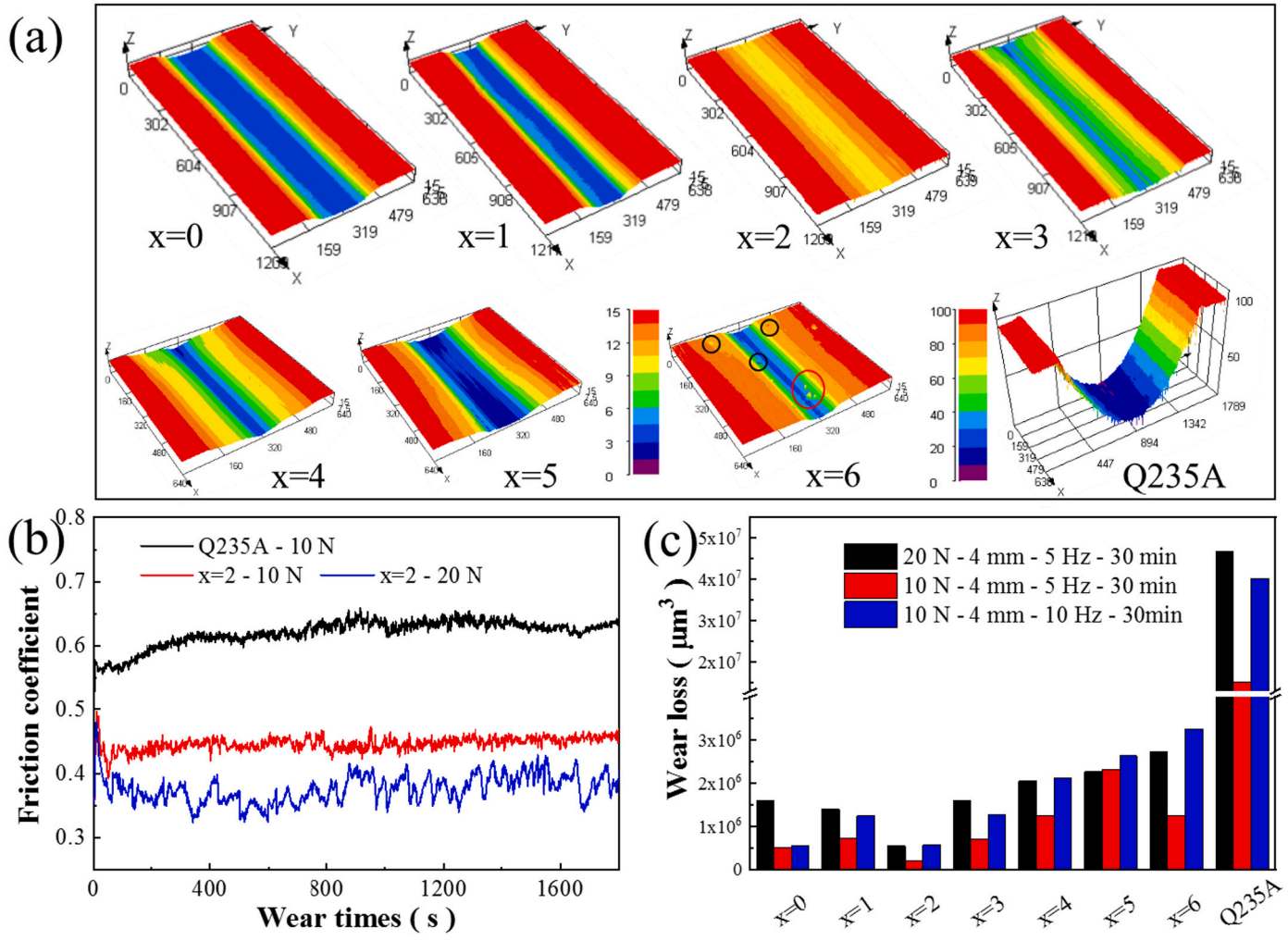

Fig. 5. (a) 3D profiles of the worn surfaces for $[(Fe_{0.6}Co_{0.2}Ni_{0.2})_{0.75-0.03x}B_{0.2}Si_{0.05+0.03x}]_{96}Nb_4$ (x = 0, 1, 2, 3, 4, 5 and 6 at.%) laser cladded coatings, as well as the Q235A steel; (b) Change of friction coefficients with wear times for the coating (x = 2) and Q235A steel; (c) The wear loss of $[(Fe_{0.6}Co_{0.2}Ni_{0.2})_{0.75-0.03x}B_{0.2}Si_{0.05+0.03x}]_{96}Nb_4$ (x = 0, 1, 2, 3, 4, 5 and 6 at.%) laser cladded coatings under different load and frequency. (For interpretation of the references to color in this figure, the reader is referred to the web version of this article.)

The friction coefficient not only reveals the contact condition of the friction pairs, but also correlates with the wear loss of the coatings. To further evaluate the wear resistance of samples, the volume lost during wear tests of the Fe-based amorphous/crystalline composite coatings with different Si content, as well as the substrate were calculated and shown in Fig. 5c. Each sample was tested at three conditions with different loading (10 N, 20 N) and reciprocating frequency (5 Hz, 10 Hz) for 30 min. The variations of wear loss at three conditions follow the same trend for the coatings with different Si contents. The value of wear loss decreases firstly when x increases from 0 to 2, and then increases with further addition of Si. This result proves that it is the Si content that contributes to the change of wear resistance for the coatings, not the testing parameters. Besides, for all of the samples, the heavier load at 20 N results in the severer wear damage, which is in accordance with the Archard's theory [33]. The $[(Fe_{0.6}Co_{0.2}Ni_{0.2})_{0.69}B_{0.2}Si_{0.11}]_{96}Nb_4$ coating shows the smallest wear loss, especially under a load of 10 N and a reciprocating frequency of 5 Hz, its wear loss is only 3.77×10^5 μm^3 after 30 min. This reveals that the wear resistance of the Fe-based amorphous/crystalline coatings can be improved by modifying the Si content. It is worthy note that the largest wear loss of the coatings is still an order of magnitude smaller than that of the Q235A steel, which confirms that the $[(Fe_{0.6}Co_{0.2}Ni_{0.2})_{0.75-0.03x}B_{0.2}Si_{0.05+0.03x}]_{96}Nb_4$ coating has excellent tribological performance.

The morphologies of the worn surfaces (10 N, 5 Hz) for the substrate and coatings are analyzed by SEM to further study the wear behavior. As shown in Fig. 6a, pervasive pits and peeling-off abrasive debris of different sizes distribute all over the worn surface of the Q235A steel, revealing the acute material removal caused by adhesive deformation. In contrary, the worn surfaces of Fe-based composite coatings are much smoother, showing a better wear resistance. For the coating with x = 0 (Fig. 6b), only a few pits appear on the worn track, which mainly come from abrasive wear. There are also several deep plowing grooves scatter near dense shallow ones, indicating that the slight adhesive wear also occurs. By increasing the Si content to x = 2, the worn surface of the coating becomes even smoother, as shown in Fig. 6c. Its wear damage is so indistinct that only a small amount of thready grooves appear at the center of worn surface. Besides, the original scratches produced from sample preparation have not been worn off and still exist on both sides of the wear track, further revealing the good wear resistance of this coating. The worn morphology of the coating with x = 2 is indicative of abrasive wear with the absence of adhesive wear. When increasing x to 5, the worn surface becomes rough again, and shows intensive shallow grooves, as well as pockmarked pits next to several fatigue cracks, as shown in Fig. 6d. This is a typical worn surface morphology from fatigue wear. The continuous increase of silicon content changes the wear mechanism of coatings into the severer abrasive wear together with the aggravating fatigue wear. Based on the above analyses of worn surfaces, proper modification of the Si content is beneficial to improve the wear resistance of coating.

4. Discussions

4.1. Elemental distribution of the coatings

In this work, $[(Fe_{0.6}Co_{0.2}Ni_{0.2})_{0.75-0.03x}B_{0.2}Si_{0.05+0.03x}]_{96}Nb_4$ (x = 0, 1, 2, 3, 4, 5 and 6 at.%) coatings are fabricated by laser cladding, while the coating with x = 2 shows the best tribological performance. To unveil the origin of the improved tribological property of the coating, analyses of elemental distribution, hardness and fracture strength of the coatings are carried out. Firstly, in order to achieve reliable tribological performance, composition segregation of the coatings should be avoided. Elemental distribution of the coating with x = 2 is studied using EDS. The EDS line scan was performed across the surface to the substrate of the coating, with the results shown in Fig. 7a and b. The composition is almost uniform through the coating, except that the iron content increases sharply at the interface between the coating and the substrate due to melting of the substrate. This further confirms the strong metallurgical bonding between coating and substrate. Besides, the top and middle parts of the coating keep the same composition as the mixed powder, indicating the uniform composition distribution across the laser cladded coating, as shown in Fig. 7b. The uniform composition distribution in the coating contributes to the excellent tribological performance of the coating with x = 2.

4.2. Hardness and fracture strength of the coatings

Coatings with good wear-resistance usually have high hardness and fracture strength. In order to evaluate the hardness of the coatings, microhardness tests are performed on the cross section of each coating, from the top surface to the bottom interface, with a step size of 0.1 mm, as

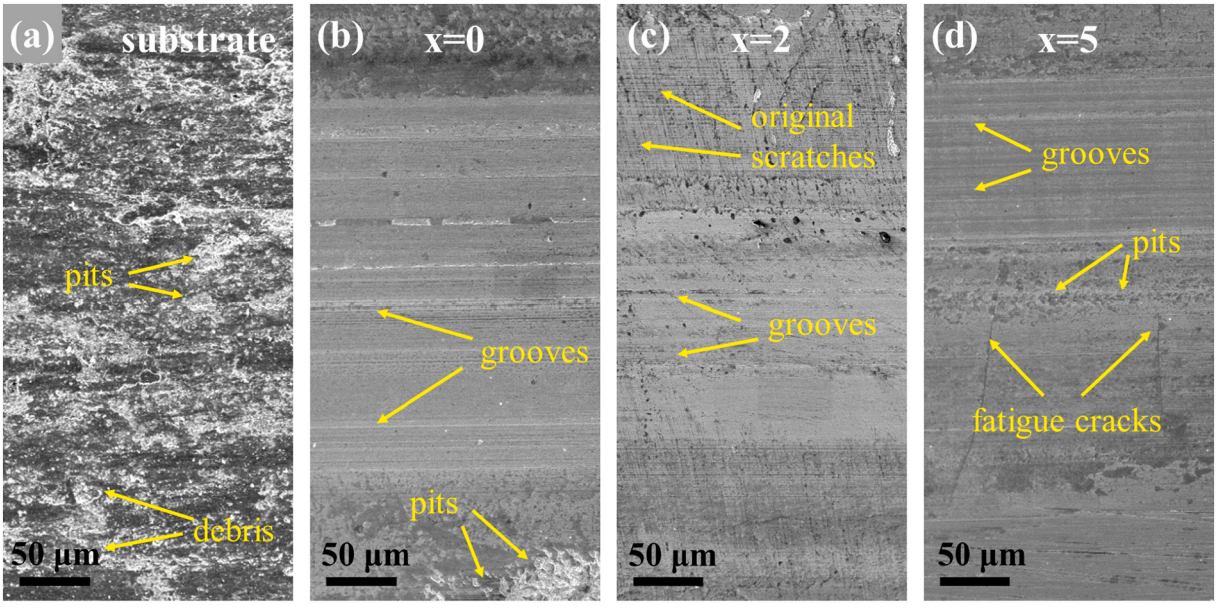

Fig. 6. SEM micrographs of the worn surfaces for the (a) Q235A substrate, as well as $[(Fe_{0.6}Co_{0.2}Ni_{0.2})_{0.75-0.03x}B_{0.2}Si_{0.05+0.03x}]_{96}Nb_4$ laser cladded coatings with (b) x = 0, (c) x = 2, (d) x = 5.

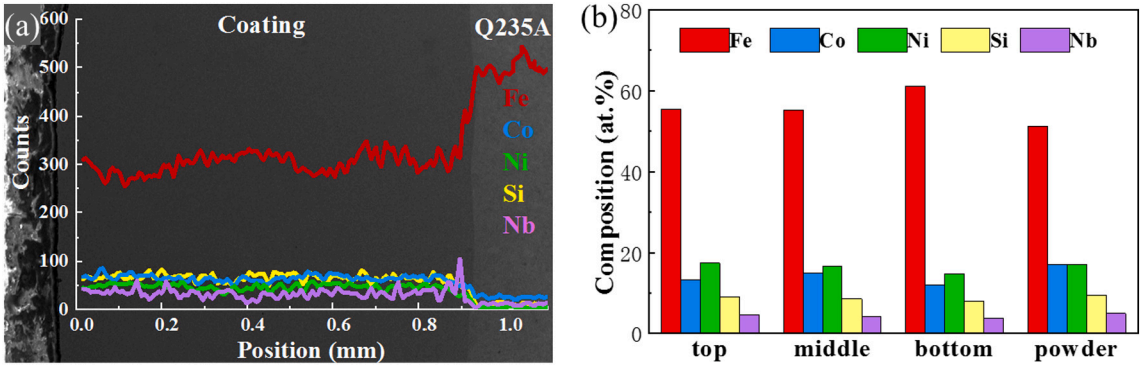

Fig. 7. (a) EDS line scan from the surface of the coating (x = 2) to the substrate; (b) The atomic compositions at the top, middle and bottom of the coating with x = 2, compared with the atomic composition of the mixed powder.

shown in Fig. 8a. The representative morphology of the indent is shown in the inset, revealing a typical Vickers hardness indentation. The thickness of the coatings is about 1 mm, thus a hardness drop can be observed at about 0.9 mm from the surface of the sample, where it comes to the interface. Clearly, the hardness of the coatings is much higher than that of the interface and the steel substrate. In order to quantitatively compare the hardness of the coatings with different Si content, the hardness values of each coating are averaged and shown in Fig. 8b. Only the values obtained at 0.1–0.8 mm from the surface are used to avoid the disturbance from the surface and interface. The average hardness of the composites is improved from 719 to 930 Hv when x increases from 0 to 2, possibly due to the increased amorphous content. Although the hardness increases continuously to 999 Hv when x = 3, the data deviation is large. This can be explained by its inhomogeneous microstructures, as shown by the solidification process analyses of DSC curves in Fig. 2. When further increase the Si content, only small variation of the hardness is observed. This is consistent with the relatively narrower solidification ranges of coatings with x = 4, 5, 6 compared with x = 3. Thus, by proper modification of Si content (x = 2), the hardness of the coatings is largely improved, and the values keep relatively even across the coating.

The fracture strength σ_f of the $[(Fe_{0.6}Co_{0.2}Ni_{0.2})_{0.75-0.03x}B_{0.2}Si_{0.05+0.03x}]_{96}Nb_4$ (x = 0, 1, 2, 3, 4, 5 and 6 at.%) coatings are measured via compressive tests, and the results are shown in Table 1. All the samples fracture at their elastic deformation region without any plastic behavior, indicating their brittle fracture under compressive loading. However, the fracture strength of all the samples are above 2100 MPa, which is much higher than the substrate. The fracture strength increases with Si addition firstly, and then decreases. The largest fracture strength reaches 2875 MPa when x = 2. Although this value is lower than the fracture strength of $[(Fe_{0.6}Co_{0.2}Ni_{0.2})_{0.75}B_{0.2}Si_{0.05}]_{96}Nb_4$ bulk metallic glass produced by copper mold casting (4160 MPa) [6], it is much higher than the Q235A steel substrate. The decrease of the strength when further increasing the Si content may come from the reduced amount of amorphous phase and the uniform microstructure.

4.3. Relationship between mechanical properties and microstructure of the coatings

The improved wear resistance, hardness and fracture strength of the Fe-based amorphous/crystalline coating with x = 2 is closely related to its microstructure. During laser cladding and solidification process, the surface of the substrate is melted and interdiffusion occurs between the substrate melt and alloy melt, forming not only a thermal gradient but also a concentration gradient in the cladding alloy. The large thermal gradient allows sufficient atomic diffusion and decreases the undercooling degree, making liquid-solid interface steady, and thus leading to the formation of planar crystallites. When the liquid-solid interface moves away from the substrate, it becomes unstable due to the increased undercooling degree. Then the cellular crystals start to form and followed by columnar crystals. However, the microstructure above the planar crystallites layer of the three coatings is quite different. With the increase of Si content, the columnar crystallites above the planar crystals disappear gradually, while the cellular crystallites form and take over the alloy. This is because Si atoms usually dissolve in the crystalline

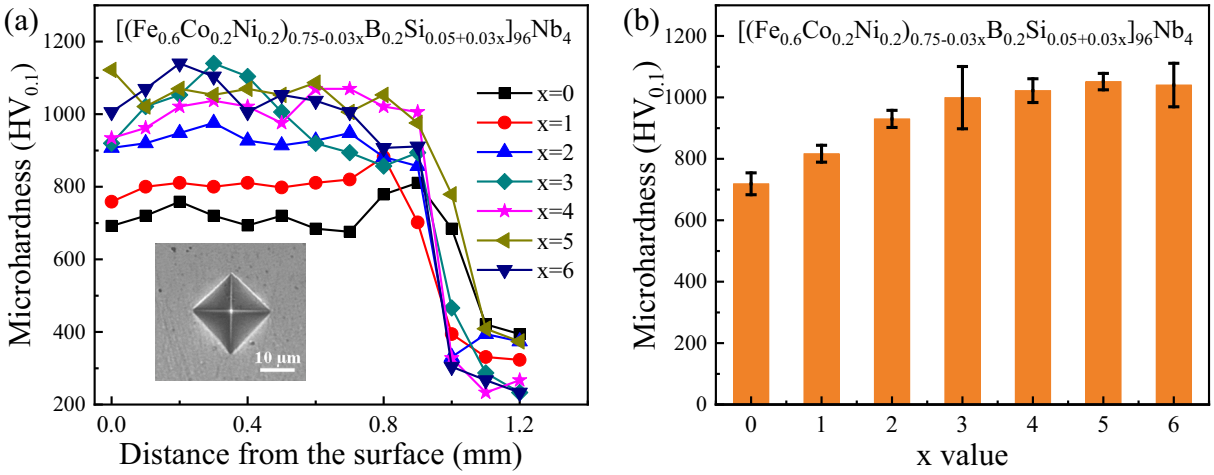

Fig. 8. (a) Vickers hardness analyses of the cross sections of $[(Fe_{0.6}Co_{0.2}Ni_{0.2})_{0.75-0.03x}B_{0.2}Si_{0.05+0.03x}]_{96}Nb_4$ (x = 0, 1, 2, 3, 4, 5 and 6 at.%) laser cladded coatings, inset shows the morphology of a representative indent; (b) The average hardness of $[(Fe_{0.6}Co_{0.2}Ni_{0.2})_{0.75-0.03x}B_{0.2}Si_{0.05+0.03x}]_{96}Nb_4$ (x = 0, 1, 2, 3, 4, 5 and 6 at.%) laser cladded coatings with error bars.

lattice of Fe, Co and Ni to form solid solution, and oversaturation of Si is reached with increasing x value, changing the undercooling degree and the solidification process. There are three existing forms of Si in the coating: some dissolve in dendrites, and some rapidly solidify as amorphous phase, while the rest usually form intermetallics and exist between dendrites. Hence Si content has enormous impacts on the microstructure of coatings, especially on the size and distribution of intermetallics [23]. When slightly increase the Si content, the GFA of the alloy is improved and the volume ratio of the amorphous phase is increased, as shown by the DSC results. With excessive addition of Si, not only the GFA decreases, but also the microstructure is more heterogeneous as revealed by the gradually enlarged ΔT_s. Thus, both the formation and growth of the dendritic grains are suppressed when $x = 2$, as shown by the SEM micrographs in Fig. 3. This variation of the thermal properties and microstructures result in the change of hardness and fracture strength of the coatings, which are important mechanical characteristics to the tribological behavior of coatings.

4.4. Origin of wear resistance for the coatings

The high hardness and fracture strength contribute to the excellent wear resistance of the coating with $x = 2$. The amorphous phase, which usually shows high hardness, serves as the reinforcement for the dendritic crystalline grains. When under loading, cracks may generate in the dendrites as they are usually softer than the amorphous phase. However, the propagation of the cracks is hindered or deflected by the hard amorphous phases, which results in energy dissipation. The proper combination of amorphous phase and crystalline dendrites leads to the high strength and hardness, and thus the wear resistance for the coatings. However, excessive addition of Si is harmful to the mechanical performance of the coatings, as the microstructure of the coatings becomes less uniform, which has been verified by the gradually increased ΔT_s. Also, the size of dendritic grains increase with excessive addition of Si, as shown in Fig. 4e. On one hand, high microstructure heterogeneity makes the soft regions easily cut or peeled off and then leads to materials removal and wear loss. On the other hand, the non-uniform structure brings the uneven distribution of the contact stress in the grinding samples, which results in the stress concentration. Thus, the large scattering of hardness values is observed when $x \geq 3$. And the fatigue cracks can be produced for the coating with $x = 5$ where the alternating shear stress is high enough, as shown in Fig. 6d. Based on the above analyses, by proper modification of the Si content, the high amorphous content and uniform microstructure can be obtained in the coating, and thus leads to the excellent tribological performance.

5. Conclusion

The effects of Si content on the microstructure, thermal and mechanical properties of laser cladded $[(Fe_{0.6}Co_{0.2}Ni_{0.2})_{0.75-0.03x}B_{0.2}Si_{0.05+0.03x}]_{96}Nb_4$ ($x = 0, 1, 2, 3, 4, 5$ and 6 at.%) amorphous/crystalline composite coatings are thoroughly studied. When $x = 2$, a $[(Fe_{0.6}Co_{0.2}Ni_{0.2})_{0.69}B_{0.2}Si_{0.11}]_{96}Nb_4$ amorphous/crystalline composite coating with high thermal stability, a Vickers hardness of 930 Hv, a high fracture strength above 2800 MPa, as well as a low wear loss of 3.77×10^5 μm^3 under a load of 10 N and a reciprocating frequency of 5 Hz after 30 min is fabricated. The GFA of the $[(Fe_{0.6}Co_{0.2}Ni_{0.2})_{0.69}B_{0.2}Si_{0.11}]_{96}Nb_4$ alloy is the largest among all the coatings as its composition is closer to eutectic point. The proper addition of Si results in the suppression of the formation and growth of dendritic grains, and also makes the microstructure across the coating more uniform. The excellent performance of the coatings in hardness, fracture strength and wear resistance of $[(Fe_{0.6}Co_{0.2}Ni_{0.2})_{0.69}B_{0.2}Si_{0.11}]_{96}Nb_4$ amorphous/crystalline composite coating is related to its high amorphous content and grain refinement. This work provides a method to improve tribological performance of Fe-based composite coating through composition modification.

CRediT authorship contribution statement

Qianqian Wang: Conceptualization, Investigation, Writing - original draft. **Xudong Bai:** Investigation, Methodology. **Bo Sun:** Writing - review & editing. **Jian Liu:** Conceptualization, Supervision. **Zhihai Cai:** Conceptualization, Supervision. **Xiubing Liang:** Conceptualization, Supervision, Project administration, Funding acquisition. **Baolong Shen:** Conceptualization, Supervision, Project administration, Funding acquisition, Writing - review & editing.

Declaration of competing interest

The authors declare that they have no known competing financial interests or personal relationships that could have appeared to influence the work reported in this paper.

Acknowledgements

This work was supported by National Natural Science Foundation of China (Grant Nos. 51631003 and 51975582), Natural Science Foundation of Jiangsu Province of China (Grant No. BK20191269), and Fundamental Research Funds for the Central Universities (Grant No. 2242019k1G005).

References

[1] X.L. Ji, C.Y. Luo, Y. Sun, J.H. Zhao, Corrosive wear of multi-layer Fe-based coatings laser cladded from amorphous powders, Wear 438 (2019) 203113.
[2] Q. Zhou, W.C. Han, Y. Du, H.X. Wu, A. Bird, X.X. Zhao, X.Z. Wang, H.F. Wang, B. Beake, Enhancing fatigue wear resistance of a bulk metallic glass via introducing phase separation: a micro-impact test analysis, Wear 436 (2019) 203037.
[3] H.S. Arora, H.S. Grewal, H. Singh, S. Mukherjee, Zirconium based bulk metallic glass-better resistance to slurry erosion compared to hydroturbine steel, Wear 307 (2013) 28–34.
[4] Z.B. Zheng, Y.G. Zheng, W.H. Sun, J.Q. Wang, Effect of heat treatment on the structure, cavitation erosion and erosion-corrosion behavior of Fe-based amorphous coatings, Tribol. Int. 90 (2015) 393–403.
[5] W.H. Wang, C. Dong, C.H. Shek, Bulk metallic glasses, Mater. Sci. Eng. R 44 (2004) 45–89.
[6] Z. Mahbooba, L. Thorsson, M. Unosson, P. Skoglund, H. West, T. Horn, C. Rock, E. Vogli, O. Harrysson, Additive manufacturing of an iron-based bulk metallic glass larger than the critical casting thickness, Appl. Mater. Today 11 (2018) 264–269.
[7] P. Gargarella, A. Almeida, R. Vilar, C.R.M. Afonso, S. Peripolli, C.T. Rios, C. Bolfarini, W.J. Botta, C.S. Kiminami, Formation of Fe-based glassy matrix composite coatings by laser processing, Surf. Coat. Technol. 240 (2014) 336–343.
[8] F.Y. Shu, Z. Tian, H.Y. Zhao, W.X. He, S.H. Sui, B. Liu, Synthesis of amorphous coating by laser cladding multi-layer Co-based self-fluxed alloy powder, Mater. Lett. 176 (2016) 306–309.
[9] L.A. Zhang, C.S. Wang, L.Y. Han, C. Dong, Influence of laser power on microstructure and properties of laser clad Co-based amorphous composite coatings, Surf. Interfaces 6 (2017) 18–23.
[10] R.F. Li, Y.J. Jin, Z.G. Li, Y.Y. Zhu, M.F. Wu, Effect of the remelting scanning speed on the amorphous forming ability of Ni-based alloy using laser cladding plus a laser remelting process, Surf. Coat. Technol. 259 (2014) 725–731.
[11] H. Wu, L.X. Liang, H. Zeng, X.D. Lan, J.G. Du, C.S. Zhou, Y. Liu, H.O. Yang, J. Li, A. H. Cai, Q.X. Li, W.D. Huang, Microstructure and nanomechanical properties of Zr-based bulk metallic glass composites fabricated by laser rapid prototyping, Mat. Sci. Eng. a-Struct. 765 (2019) 138306.
[12] J. Kim, K. Kang, S. Yoon, S. Kumar, H. Na, C. Lee, Oxidation and crystallization mechanisms in plasma-sprayed Cu-based bulk metallic glass coatings, Acta Mater. 58 (2010) 952–962.
[13] L.M. Zhang, S.D. Zhang, A.L. Ma, H.X. Hu, Y.G. Zheng, B.J. Yang, J.Q. Wang, Influence of sealing treatment on the corrosion behavior of HVAF sprayed Al-based amorphous/nanocrystalline coating, Surf. Coat. Technol. 353 (2018) 263–273.
[14] C.C. Sun, X.L. Zhou, C. Xie, L.L. Xu, R.Z. Li, B.B. Liu, Formation of Al-based amorphous/nanocrystalline coatings by cold spraying, Surf. Coat. Technol. 389 (2020).
[15] X.D. Lan, H. Wu, Y. Liu, W.D. Zhang, R.D. Li, S.Q. Chen, X.F. Zai, T. Hu, Microstructures and tribological properties of laser cladded Ti-based metallic glass composite coatings, Mater. Charact. 120 (2016) 82–89.
[16] X.B. Liang, J.B. Cheng, Y. Feng, Y.X. Chen, B.S. Xu, Research progress on Fe-based amorphous coatings, J. Mater. Eng. 45 (2017) 1–12.
[17] C. Zhang, W. Wang, Y.-C. Li, Y.-G. Yang, Y. Wu, L. Liu, 3D printing of Fe-based bulk metallic glasses and composites with large dimensions and enhanced toughness by thermal spraying, J. Mater. Chem. A 6 (2018) 6800–6805.
[18] C. Zhang, W. Wang, W. Xing, L. Liu, Understanding on toughening mechanism of bioinspired bulk metallic glassy composites by thermal spray additive manufacturing, Scr. Mater. 177 (2020) 112–117.

[19] E. Williams, N. Lavery, Laser processing of bulk metallic glass: a review, J. Mater. Process. Technol. 247 (2017) 73–91.
[20] S. Pauly, L. Löber, R. Petters, M. Stoica, S. Scudino, U. Kühn, J. Eckert, Processing metallic glasses by selective laser melting, Mater. Today 16 (2013) 37–41.
[21] Q.J. Zhu, S.Y. Qu, X.H. Wang, Z.D. Zou, Synthesis of Fe-based amorphous composite coatings with low purity materials by laser cladding, Appl. Surf. Sci. 253 (2007) 7060–7064.
[22] A. Basu, A.N. Sarnant, S.P. Harirnkar, J.D. Majumdar, I. Manna, N.B. Dahotre, Laser surface coating of Fe-Cr-Mo-Y-B-C bulk metallic glass composition on AISI 4140 steel, Surf. Coat. Technol. 202 (2008) 2623–2631.
[23] P. Zhang, H. Yan, C. Yao, Z. Li, Z. Yu, P. Xu, Synthesis of Fe–Ni–B–Si–Nb amorphous and crystalline composite coatings by laser cladding and remelting, Surf. Coat. Technol. 206 (2011) 1229–1236.
[24] P.L. Zhang, Y.L. Lu, H. Yan, K. Ma, P.Q. Xu, Z.S. Yu, Y.Y. Chen, M. Ding, Effect of Nb addition on Fe-Ni-B-Si amorphous and crystalline composite coatings by laser processing, Surf. Coat. Technol. 236 (2013) 84–90.
[25] X.Y. Ye, Y.C. Shin, Synthesis and characterization of Fe-based amorphous composite by laser direct deposition, Surf. Coat. Technol. 239 (2014) 34–40.
[26] S.L. Wang, Z.Y. Zhang, Y.B. Gong, G.M. Nie, Microstructures and corrosion resistance of Fe-based amorphous/nanocrystalline coating fabricated by laser cladding, J. Alloys Compd. 728 (2017) 1116–1123.
[27] A. Takeuchi, A. Inoue, Classification of bulk metallic glasses by atomic size difference, heat of mixing and period of constituent elements and its application to characterization of the main alloying element, Mater. Trans. 46 (2005) 2817–2829.
[28] B.L. Shen, A. Inoue, C.T. Chang, Superhigh strength and good soft-magnetic properties of (Fe, Co)-B-Si-Nb bulk glassy alloys with high glass-forming ability, Appl. Phys. Lett. 85 (2004) 4911–4913.
[29] H. Rietveld, Line profiles of neutron powder-diffraction peaks for structure refinement, Acta Crystallogr. 22 (1967) 151–152.
[30] H. Ma, L.L. Shi, J. Xu, Y. Li, E. Ma, Discovering inch-diameter metallic glasses in three-dimensional composition space, Appl. Phys. Lett. 87 (2005), 181915.
[31] M. Yang, X.J. Liu, Y. Wu, H. Wang, X.Z. Wang, Z.P. Lu, Unusual relation between glass-forming ability and thermal stability of high-entropy bulk metallic glasses, Mater. Res. Lett. 6 (2018) 495–500.
[32] J.B. Cheng, X.B. Liang, Z.H. Wang, B.S. Xu, Dry sliding friction and wear properties of metallic glass coating and martensite stainless coating, Tribol. Int. 60 (2013) 140–146.
[33] J.F. Archard, Contact and rubbing of flat surfaces, J. Appl. Phys. 24 (1953) 981–988.